THE JOURNAL OF PHYSICAL CHEMISTRY Letters

pubs.acs.org/JPCL Letter

MAI Termination Favors Efficient Hole Extraction and Slow Charge Recombination at the $MAPbI_3$/CuSCN Heterojunction

Jinlu He, David Casanova, Wei-Hai Fang, Run Long,* and Oleg V. Prezhdo

Cite This: *J. Phys. Chem. Lett.* 2020, 11, 4481–4489

Read Online

ACCESS | Metrics & More | Article Recommendations | Supporting Information

ABSTRACT: Photoinduced charge separation is the key step determining the efficiency of photon-to-electron conversion in solar cells, while charge carrier lifetimes govern the overall solar cell performance. Experiments report that copper(I) thiocyanate (CuSCN) is a very promising hole extraction layer for perovskite solar cells. Using nonadiabatic molecular dynamics combined with *ab initio* time-domain density functional theory, we show that termination of $CH_3NH_3PbI_3$ ($MAPbI_3$) at $MAPbI_3$/CuSCN heterojunctions has a strong influence on both charge separation and recombination. Both processes are favored by MAI termination, compared to PbI_2 termination. Because the $MAPbI_3$ valence band originates from iodine orbitals while the conduction band arises from Pb orbitals, MAI termination places holes close to CuSCN, favoring extraction, and creates an MAI barrier for recombination of electrons in $MAPbI_3$ and holes in CuSCN. The opposite is true for PbI_2 termination. The origin of these effects is attributed solely to the properties of the $MAPbI_3$ surfaces, and therefore, the conclusions should apply to other hole-transporting materials and can be generalized to other perovskites. Importantly, the simulations show that the injected hole remains hot for several hundreds of femtoseconds, allowing it to escape the interfacial region and prevent formation of bound excitons. This study suggests that metal halide perovskites should be treated with an organic precursor, such as MAI, prior to the formation of their interfaces with hole-transporting materials. The reported results advance the fundamental understanding of the highly unusual properties of metal halide perovskites and provide specific guidelines for optimizing the performance of perovskite solar cells and other devices.

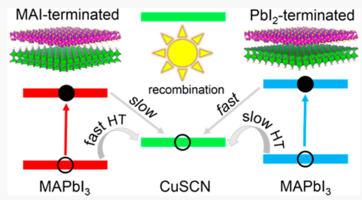

Hybrid organic–inorganic perovskites (HOIPs) are intensely studied due to their high absorption coefficients,[1] tunable bandgaps,[2] long carrier lifetimes, and large diffusion lengths,[3] motivating HOIP applications in many areas, including light-emitting diodes,[4] optically pumped lasers,[5] photocatalytic water-splitting assemblies,[6] and solar cells.[7−10] The power conversion efficiencies (PCEs) of perovskite solar cells have increased rapidly within just 10 years, from 3.8%[11] in 2009 to the recently certified value of 25.2%.[12] Although the PCEs have reached commercially viable values, the high-PCE devices employ organic hole-transporting materials (HTMs), such as 2,2′,7,7′-tetrakis(*N*,*N*-di-*p*-methoxyphenyl-amine)-9,9′-spirobifluorene (spiro-MeOTAD)[13] and poly(triarylamine) (PTAA).[14] The relatively high cost and low thermal stability of these HTMs limit their potential for large-scale applications. Compared with organic HTMs, inorganic HTMs are ideal alternates because of their low cost, high stability, and ease of synthesis.[15]

Recently, many experiments have reported applications of inorganic HTMs, such as NiO,[16] CuI,[17] and copper(I) thiocyanate (CuSCN),[18−21] in perovskite solar cells. CuSCN is an excellent HTM, having high hole mobility, good thermal stability, and a well-aligned work function.[22] Arora et al. have demonstrated >20% PCEs of perovskite solar cells with CuSCN as the HTM.[18] They have also shown that the stability of the CuSCN-based devices is better than that of spiro-OMeTAD perovskite solar cells.[18,23] The superior performance of perovskite/CuSCN heterojunctions may be related to surface termination of $MAPbI_3$, which determines the efficiency of hole extraction and the time scale of electron–hole recombination, both of which are crucial for device optimization. Termination of $MAPbI_3$ surfaces can be controlled by varying the excess precursor solution during the synthesis. Experiments show that excess MAI[24] and PbI_2[25] precursors lead to the formation of MAI- and PbI_2-terminated surfaces, respectively. Mosconi et al. have shown that PbI_2 termination can enhance the electronic coupling at $MAPbI_3$/TiO_2 heterojunctions, compared to MAI termination, resulting in faster electron transfer from $MAPbI_3$ to TiO_2.[25] Beljonne and co-workers have demonstrated that surface termination of $MAPbI_3$ greatly influences the energy level alignment in $MAPbI_3$/C60 heterojunctions.[26] The experimental and theoretical findings presented above indicate that termination of $MAPbI_3$ can have a significant influence on the properties of heterojunctions and provide a means of controlling carrier separation and recombination dynamics. These considerations,

Received: May 13, 2020
Accepted: May 18, 2020
Published: May 18, 2020

together with the practical importance of the CuSCN HTM, call for a detailed microscopic analysis of the influence of $MAPbI_3$ termination on charge transfer and recombination at perovskite/CuSCN heterojunctions.

In this Letter, we use time-domain *ab initio* simulations to demonstrate that termination of the $MAPbI_3$ interface with CuSCN has a strong influence on both hole extraction and electron−hole recombination. By considering MAI- and PbI_2-terminated $MAPbI_3$, we show that MAI termination is more favorable for both processes, strongly indicating that $MAPbI_3$ should be treated with MAI prior to the formation of interfaces with HTMs. The origins of these effects are attributed solely to the properties of the $MAPbI_3$ surfaces, and therefore, they should apply to not only CuSCN but also other HTMs. In addition, the reported findings should apply to other metal halide perovskites, in which MA, Pb, and/or I is replaced with other species. The mechanism rationalizing the extended charge recombination time is independent of whether MA is replaced with another organic or inorganic cation, while the hole transfer efficiency depends on the properties of the organic cation, such as MA, FA, or GA. Specifically, the photoinduced hole transfer at the MAI-terminated $MAPbI_3$/CuSCN interface is more efficient than at the PbI_2-terminated interface, because the hole is localized on the iodine atoms present in the MAI termination, and because rapid motions of the light atoms of the organic cations produce frequent crossings of donor and acceptor energy levels. Notably, the hole remains hot for 200−300 fs after the injection, and therefore, it can move rapidly away from the interface prior to interacting with the remaining electron and forming a bound state. This situation is particularly important for organic HTMs, which allow the formation of strongly bound excitons. The electron−hole recombination is slower for the MAI-terminated interface, because the electron remaining in $MAPbI_3$ is located farther from the interface, reducing the level of overlap of electron and hole wave functions, and because the PbI_2-terminated interface exhibits stronger chemical interactions with CuSCN. The detailed atomistic insights provided by the state-of-the-art non-equilibrium simulations broaden our fundamental understanding of the fascinating properties of metal halide perovskites and provide specific guidelines for improving the performance of perovskite solar cells and related devices.

The MAI- and PbI_2-terminated $MAPbI_3$/CuSCN heterojunctions are shown in Figure 1. They are constructed with a 128-atom CuSCN (2×2)(010) surface and a 144-atom $MAPbI_3$ (2×3)(001) surface. The lattice mismatch between the two materials is modest, 2.9% and 7.6% along the *x*- and *y*-axes, respectively, allowing us to model the heterojunction with fewer than 300 atoms. Because the periodic boundary conditions are used in all three directions, a vacuum region of 30 Å is added along the heterojunction normal, to separate spurious interactions between heterojunction images.

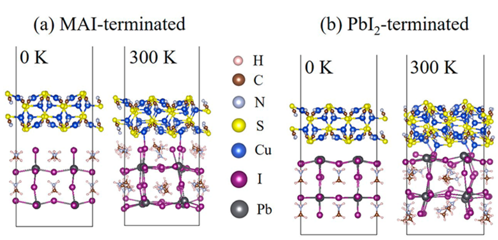

Figure 1. Simulation cells of (a) MAI- and (b) PbI_2-terminated $MAPbI_3$/CuSCN heterojunctions in the optimized geometry at 0 K and a representative snapshot at 300 K. The materials maintain a nearly perfect periodic structure at 0 K, and the interactions at the interface are purely van der Waals. Significant distortions are observed at the interface at 300 K. The formed Cu−I bonds are shorter for the PbI_2 termination, because motions of MA cations help to maintain the $MAPbI_3$−CuSCN separation for the MAI termination.

The *ab initio* nonadiabatic (NA) molecular dynamics (MD) simulations of the charge separation and recombination processes are carried out using the fewest switching surface hopping (FSSH) technique[27−29] implemented within time-dependent density functional theory (TD-DFT) in the Kohn−Sham (KS) framework.[30,31] The heavier and slower nuclei, including all types of atoms (H, C, N, S, I, Cu, and Pb), are treated (semi)classically, while the lighter and faster electrons are described using quantum mechanics. The quantum decoherence correction to FSSH[32] is used in the electron−hole recombination simulation,[33−35] because the recombination time is much longer than the decoherence time. The decoherence time is computed by the second-order cumulant approximation of the optical response theory.[36,37] The approach has been applied successfully to study photoexcitation dynamics in a broad range of systems, including perovskites[38−54] and many other materials.[55−69] A detailed description of the theoretical methodology can be found in refs 29 and 70.

The geometry optimization, adiabatic MD, and NA coupling calculations are performed with the Vienna *ab initio* Simulation Package (VASP).[71] The electron exchange-correlation effects and electron−ion core interactions are described with the Perdew−Burke−Ernzerhof (PBE) functional[72] and projector-augmented wave (PAW) method,[73] respectively. The plane-wave basis energy cutoff is 400 eV. The calculations are carried out using the Γ-centered 2 × 2 × 1 Monkhorst−Pack k-point mesh. To obtain accurate electronic structure, a denser 8 × 8 × 1 k-point mesh is employed.[74] The van der Waals interactions are described with Grimme's DFT-D3 approach.[75] The dipole correction is taken into account for all calculations.

After geometry optimization, the two systems are heated to 300 K by velocity rescaling. Then, 6 ps microcanonical ensemble trajectories are generated with a 1 fs time step and used for the NA coupling calculations. The 1000 configurations from the first picosecond of the 6 ps trajectories are used as initial configurations for the NAMD calculations. The hole transfer dynamics is modeled with FSSH,[28] while electron−hole recombination is studied with decoherence-corrected FSSH.[32] We scale the band offset at the heterojunction to the experimental value[20] during the electron−hole recombination simulations.

Figure 1 shows the optimized geometries of the MAI- and PbI_2-terminated $MAPbI_3$/CuSCN interfaces, as well as representative geometries chosen from the MD trajectories performed at room temperature. At 0 K, the CuSCN and $MAPbI_3$ layers exhibit minor distortions at the interface, the organic cations of $MAPbI_3$ are arranged in an orderly manner, and the interaction between the two materials is purely van der Waals. When the systems are heated to ambient temperature, the geometry of the $MAPbI_3$/CuSCN interfacial region is notably distorted, and the organic cations of $MAPbI_3$ become disordered. The geometry distortion leads to the formation of Cu−I bonds across the interface. The average Cu−I bond lengths in the MAI- and PbI_2-terminated heterojunctions are

https://dx.doi.org/10.1021/acs.jpclett.0c01467
J. Phys. Chem. Lett. 2020, 11, 4481−4489

2.711 and 2.671 Å, respectively. The distance is larger for the MAI-terminated interface, because rotational motions of the MA cations help to maintain the $MAPbI_3$−CuSCN separation. The shorter Cu−I bond length indicates that interactions between the two slabs are stronger in the PbI_2-terminated system. This factor plays an important role in electron−hole recombination.

To further investigate the influence of $MAPbI_3$ termination on nuclear dynamics, we computed the root-mean-square displacement velocity of atoms in the MAI- and PbI_2-terminated $MAPbI_3$/CuSCN heterojunctions. The average velocities are calculated for the combined system and separately for CuSCN and $MAPbI_3$ (Table 1). The data show that atoms in the PbI_2-terminated system move faster on avergae than in the MAI-terminated system. Interestingly, this difference arises from the CuSCN subsystem. The average velocity of the atoms in CuSCN is 5 times larger for the PbI_2 termination than for the MAI termination. This is because the CuSCN structure becomes less stable at the interface, and CuSCN forms transient bonds with the perovskite, causing a significant exchange of energy between the potential (bonding) and kinetic (velocity) components.

Table 1. Root-Mean-Square Atomic Velocities (angstroms per femtosecond) in the MAI- and PbI_2-Terminated $MAPbI_3$/CuSCN Heterojunctions

	total[a]	CuSCN[b]	$MAPbI_3$[c]
MAI-terminated	0.031	0.004	0.054
PbI_2-terminated	0.036	0.020	0.051

[a]Averaged over all atoms. [b]Averaged over atoms in CuSCN. [c]Averaged over atoms in $MAPbI_3$.

Panels a and b of Figure 2 show the projected density of states (PDOS) of the MAI- and PbI_2-terminated $MAPbI_3$/CuSCN heterojunctions, respectively. The PDOS displays a type II band alignment between CuSCN and $MAPbI_3$, favoring hole transfer to CuSCN and electron transfer to $MAPbI_3$. Generally, the PBE functional gives good agreement with the experimental bandgaps in HOIPs.[76,77] However, PBE underestimates the bandgaps of other materials, including TiO_2[78] and CuSCN.[79] Estimated on the basis of the PDOS, the $MAPbI_3$ bandgaps in the MAI- and PbI_2-terminated heterojunctions are 1.70 and 1.95 eV, respectively. These values are close to the value of 1.70 eV determined experimentally for the $MAPbI_3$ (001) surface.[80] The difference in the bandgaps for the MAI and PbI_2 interfaces arises due to the variation of the interfacial interactions. The CuSCN bandgaps in the MAI- and PbI_2-terminated systems differ little and are 2.35 and 2.33 eV, respectively. They are smaller than the experimental bandgap[20] of pure CuSCN due to the PBE self-interaction error. The bandgaps of the MAI- and PbI_2-terminated heterojunctions, computed as the difference between the $MAPbI_3$ HOMO and CuSCN LUMO, are 1.46 and 1.65 eV, respectively. This is in good agreement with the experimental value of 1.40 eV,[20] indicating that the energy level alignment between CuSCN and $MAPbI_3$ is appropriate for further calculations.

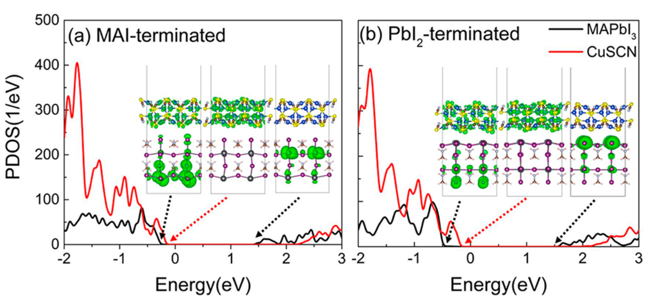

Figure 2. Projected density of states (PDOS) of (a) MAI- and (b) PbI_2-terminated $MAPbI_3$/CuSCN heterojunctions. Charge densities of the key orbitals involved in the hole transfer and electron−hole recombination processes are shown in the insets. The zero energy is set to the Fermi level. Holes in $MAPbI_3$ are supported by iodine atoms. Direct contact of iodines with CuSCN, as well as participation of high-frequency MA motions, facilitates rapid hole transfer from $MAPbI_3$ to CuSCN for MAI termination. Electrons in $MAPbI_3$ are supported by Pb atoms. The spatial separation of the $MAPbI_3$ electrons from the CuSCN holes at the MAI-terminated interface favors slow charge recombination.

The charge densities of the key orbitals involved in the photoinduced hole transfer and electron−hole recombination processes are shown in the insets of Figure 2. The hole is transferred from the $MAPbI_3$ HOMO, which is delocalized slightly onto CuSCN, to the CuSCN HOMO, which is fully localized on CuSCN. The delocalization of the $MAPbI_3$ HOMO onto CuSCN facilitates the hole transfer, because the hole donor state overlaps with the hole acceptor state. In contrast, the electron−hole recombination takes place between the CuSCN HOMO and the $MAPbI_3$ LUMO, both of which are fully localized within the corresponding subsystems. There is little overlap between these orbitals. As a result, the level of NA coupling between these states is very low, on the order of 1 meV (Table 2), and the recombination is slow. In addition, the $MAPbI_3$ LUMO is localized away from the interface for the MAI termination (Figure 2a) while it is localized at the interface for the PbI_2 termination (Figure 2b). This fact favors slower charge recombination for the MAI-terminated interface, which therefore is preferable over the PbI_2-terminated heterojunction.

Table 2. Experimental Bandgaps, Absolute Averaged Values of NA Coupling, Pure-Dephasing Times, and Nonradiative Electron−Hole Recombination Times for the MAI- and PbI_2-Terminated $MAPbI_3$/CuSCN Heterojunctions

	bandgap (eV)	NA coupling (meV)	dephasing (fs)	time (ps)
MAI-terminated	1.40	0.93	4.36	487
PbI_2-terminated	1.40	1.56	2.48	240

The photoinduced hole transfer in the perovskite/CuSCN heterojunctions occurs from the $MAPbI_3$ HOMO to the CuSCN valence band (VB). The donor state undergoes frequent crossings with the (quasi)continuous manifold of acceptor states. The crossings are driven by fluctuations in the system geometry, and therefore, the involvement of higher-frequency modes would increase the number of donor−acceptor level crossings and accelerate the hole transfer. In addition, after the transfer, the hole relaxes to the CuSCN HOMO, which is offset from the $MAPbI_3$ HOMO by 0.2−0.3 eV, depending on the $MAPbI_3$ termination (Figure 2). Note that the energy offset increases by ∼0.1 eV at ambient temperature, as discussed below. The hole energy is transferred to vibrations and is released as heat. The energy transfer from

https://dx.doi.org/10.1021/acs.jpclett.0c01467
J. Phys. Chem. Lett. 2020, 11, 4481−4489

the hole to vibrations is most efficient under resonance conditions; 0.2 eV corresponds to ∼1600 cm^{-1} in wavenumber units, and therefore, participation of vibrations with the corresponding frequencies would accelerate the relaxation.

To characterize the phonon modes that couple to the hole transfer, we compute Fourier transforms (FTs) of the autocorrelation functions of phonon-induced fluctuations in the energy gaps between the donor and acceptor states. The autocorrelation functions are defined as $C_{ij}(t) = \langle \delta E_{ij}(t')\delta E_{ij}(t - t')\rangle_{t'}$, where the brackets denote canonical averaging. $\delta E_{ij}(t)$ represents the fluctuation of energy gap between states i and j from the average value. The FTs, computed as $I(\omega) = \left|\frac{1}{\sqrt{2\pi}}\int_{-\infty}^{\infty} dt e^{-i\omega t} C_{ij}(t)\right|^2$, known as influence spectra or spectral densities, are shown in Figure 3 for the two

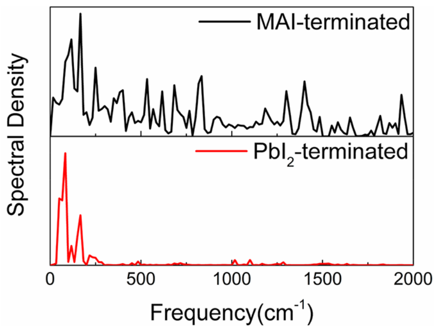

Figure 3. Spectral densities for the hole transfer, computed as Fourier transforms of fluctuations of the energy gaps between the $MAPbI_3$ and CuSCN HOMOs in the MAI- and PbI_2-terminated heterojunctions. The participation of a broad range of vibrations in the MAI-terminated heterojunction accelerates charge separation.

terminations. The spectra are notably different at frequencies of >250 cm^{-1}. In particular, multiple vibrations up to 2000 cm^{-1} couple to the hole transfer for the MAI-terminated interface. No such signals are seen in the influence spectrum for the PbI-terminated case. The difference stems from the fact that the hole has to pass though the region occupied by the MA molecules for the MAI termination. These molecules are made of light atoms that vibrate at high frequencies. Even though the orbitals of the MA cations do not contribute to the states that support electrons and holes in the $MAPbI_3$/CuSCN heterojunction, the cations influence the charge dynamics through electrostatic interactions. No such effect is seen for the PbI_2 termination. This result demonstrates that the MAI termination is favorable for achieving rapid charge separation across in $MAPbI_3$/CuSCN interface, although the MAI termination also accelerates relaxation of the hole to the CuSCN HOMO.

The largest contributions to the influence spectra shown in Figure 3 come from slow vibrations with frequencies of <250 cm^{-1}. The peaks below 120 cm^{-1} can be attributed to vibrations of the inorganic Pb−I octahedron.[81] The peaks between 120 and 200 cm^{-1} can be ascribed to librations of the organic cations.[81] The peaks at 200 and 240 cm^{-1} arise from the Cu−S and Cu−N stretching vibrations, respectively.[82] The peaks near 430 cm^{-1} correspond to SCN group bending.[82] The peaks at ∼750 cm^{-1} can be assigned to the C−S stretching.[82] The peaks near 2000 cm^{-1} can be ascribed to the vibration of the CN group.[82]

Figure 4 presents two-dimensional (2D) maps of NA couplings between all pairs of orbitals involved in the

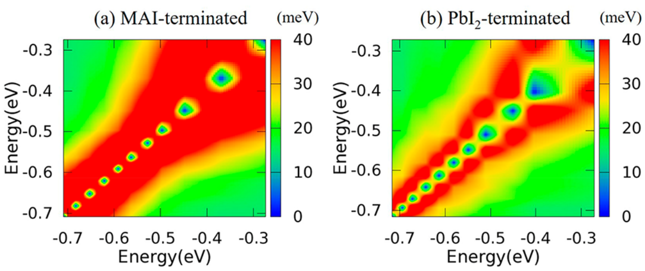

Figure 4. Two-dimensional visualization of the average NA couplings between VB orbitals for the hole transfer in (a) MAI- and (b) PbI_2-terminated $MAPbI_3$/CuSCN heterojunctions. Larger NA couplings lead to faster hole transfer in the MAI-terminated heterojunction. The zero energy is set to the VB maximum, and the x- and y-axes refer to the energies of VB orbitals.

photoinduced hole transfer. We calculated the NA coupling d_{ij} numerically as the overlap of KS orbitals i and j at sequential time steps:

$$d_{ij} = -i\hbar\langle \phi_i|\nabla_R|\phi_j\rangle\cdot\dot{\mathbf{R}} = -i\hbar\left\langle \phi_i\left|\frac{\partial}{\partial t}\right|\phi_j\right\rangle$$
$$= -i\hbar\frac{\left\langle \phi_i(t)\left|\frac{\partial}{\partial t}\right|\phi_j(t+\Delta t)\right\rangle - \left\langle \phi_i(t+\Delta t)\left|\frac{\partial}{\partial t}\right|\phi_j(t)\right\rangle}{2\Delta t}$$

The many-electron wave functions are constructed from the KS orbitals, and the NA couplings between the many-electron wave functions are related to the NA couplings between the orbitals, as described in detail in ref 29. Figure 4 refers to the hole transfer process, which occurs within the manifold of VB states. The electron remains at the bottom of the conduction band (CB), and the NA couplings between the many-electron wave functions are determined directly by the NA couplings between the VB orbitals, as represented in Figure 4. The 2D color map indicates the strength of the NA coupling. The x- and y-axes represent orbital energies relative to the VB maximum, the energy of which is set to 0.

The NA couplings are stronger for the MAI-terminated system, indicating that such termination is more suitable for charge separation. The blue dots on the diagonal of Figure 4 represent zeros, because the first-order NA couplings used in these calculations vanish on the diagonal.[83] Interestingly, the NA couplings between states that are close in energy are notably larger than the couplings between more distant states. This observation indicates that hops between nearest neighbor orbitals are more likely than transitions leading to the exchange of large amounts of energy between charges and vibrations. The result is consistent with the fact that low-frequency modes contribute most strongly to hole transfer and relaxation (Figure 3). The average absolute values of the NA coupling between the nearest neighbor states are 84.93 and 54.19 meV for the MAI- and PbI_2-terminated interfaces, respectively. The corresponding data for each pair of states are listed in Table S1. The NA values demonstrate that the MAI termination is more favorable for charge separation.

Figure 5 presents time-dependent data from NAMD characterizing the photoinduced hole transfer from $MAPbI_3$ to CuSCN in the MAI- and PbI_2-terminated systems, as well as nonradiative hole relaxation to the CuSCN VB edge. The

https://dx.doi.org/10.1021/acs.jpclett.0c01467
J. Phys. Chem. Lett. 2020, 11, 4481−4489

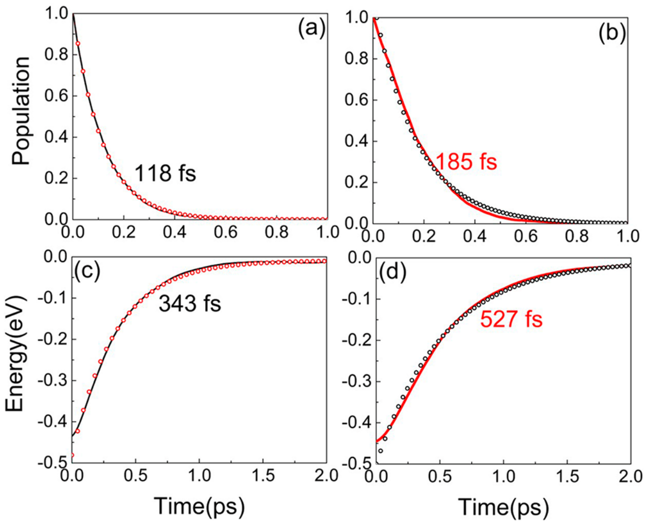

Figure 5. Hole transfer for (a) MAI- and (b) PbI_2-terminated $MAPbI_3$/CuSCN heterojunctions. (c and d) Corresponding energy decay. Hole transfer is faster for the MAI than for the PbI_2 termination. Importantly, the energy losses are slower than charge separation. The transferred hole remains hot for 200−300 fs, which is favorable for solar cell applications.

population curves shown in Figure 5 are fitted with the exponential function $P(t) = \exp(-t/\tau)$. The energy curves are fitted with the equation $E(t) = E(0)\ \exp(-t/\tau)$. The average initial energy of the hole, $E(0)$, is negative and calculated relative to the VB maximum that is set to 0 eV. Hole transfer is faster than energy relaxation in both systems (compare parts a and b with parts c and d of Figure 5). The simulations show that the hole remains hot for 200−300 fs after the charge separation. This fact has a positive effect on long-range charge separation and transport, because hot holes can travel faster inside CuSCN than fully relaxed holes.

The initial values of the energy relaxation curves in panels c and d of Figure 5 represent the canonically averaged offsets between the VB edges of the two materials. The canonically averaged VB edge offsets are 0.43 and 0.45 eV for the MAI- and PbI_2-terminated interfaces, respectively, and are larger than the corresponding values for the optimized geometries (Figure 2). The 0.1−0.2 eV difference indicates that thermal disorder cannot be neglected when estimating driving forces for charge transfer processes in heterostructures designed for solar energy harvesting.

To design high-performance solar cells, one needs to ensure slow electron−hole recombination, because it is the major pathway for charge and energy losses. Having established that the MAI termination is preferred over the PbI_2 termination for efficient charge separation, we investigate whether the $MAPbI_3$ surface termination has an effect on electron−hole recombination. The charge densities of the electron and hole states involved in the recombination exhibit little overlap (insets of Figure 2). Moreover, the $MAPbI_3$ LUMO supporting the electron is localized away from the interface for MAI termination, compared to PbI_2 termination, suggesting that the former is preferrable for long-lived charge separation. The NA coupling value for the charge recombination (Table 2) confirms this conclusion. It is smaller for MAI than for PbI_2 termination.

Next, we characterize the vibrational modes that couple the excited and ground states and promote the nonradiative relaxation. In a manner similar to that of charge separation (Figure 3), we compute FTs of phonon-induced fluctuations of the bandgap in the MAI- and PbI_2-terminated heterojunctions. Figure 6 shows that low-frequency vibrations in the 30−200 cm^{-1} region induce relaxation. The peaks at 33 and 66 cm^{-1} can be attributed to vibrational motions of the inorganic Pb−I octahedra.[81] The peaks near 133 cm^{-1} can be ascribed to librations of the organic cations.[81] The dominant peak is more intense in the PbI_2-terminated heterojunction, indicating stronger electron−phonon coupling and faster recombination.

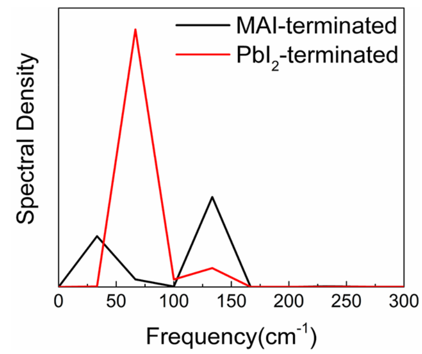

Figure 6. Spectral densities for electron−hole recombination, obtained as Fourier transforms of fluctuations of the bandgaps in the MAI- and PbI_2-terminated $MAPbI_3$/CuSCN heterojunctions. Low-frequency vibrations dominate the spectra. A higher intensity of the main peak for PbI_2 termination reflects stronger electron−phonon interactions, leading to faster nonradiative electron−hole recombination.

The pure-dephasing functions for the HOMO−LUMO transition characterize quantum coherence loss during the nonradiative charge recombination. They are calculated via the second-order cumulant approximation of the optical response theory[36,37] and are shown in Figure 7. The decoherence times, listed in Table 2, are acquired by fitting the curves with a Gaussian, $\exp[-0.5(t/\tau)^2]$. Note that decoherence is a time-domain equivalent of the Franck−Condon factor defined in the energy domain[84,85] and that electron−phonon coupling can be quantified by the Huang−Rhys factor.[86] The 2−4 fs decoherence times are very short, compared to those calculated for other nanoscale materials.[87−93] Short coherence manifests itself in the so-called quantum Zeno effect,[94] according to which the quantum transition becomes very slow. Thus, the short quantum coherence times seen with

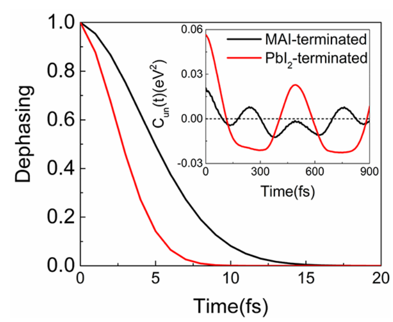

Figure 7. Pure-dephasing functions for electron−hole recombination in the MAI- and PbI_2-terminated $MAPbI_3$/CuSCN heterojunctions. The inset presents the unnormalized autocorrelation functions of the energy gap fluctuations.

perovskites contribute to long charge carrier lifetimes and high solar cell efficiencies.

Finally, we carry out the NAMD simulations of the nonradiative electron−hole recombination in the MAI- and PbI_2-terminated $MAPbI_3$/CuSCN heterojunctions. The evolution of the excited state populations is displayed in Figure 8.

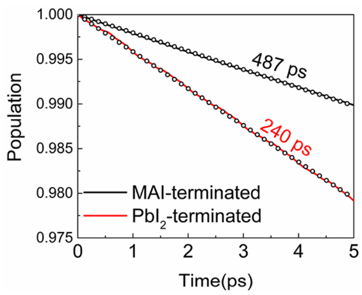

Figure 8. Electron−hole recombination dynamics in the MAI- and PbI_2-terminated $MAPbI_3$/CuSCN heterojunctions. Charge carriers live longer for MAI termination.

The recombination times, listed in Table 2, are obtained by fitting the curves with the short time linear approximation of the exponential decay, $P(t) = \exp(-t/\tau) \approx 1 - t/\tau$. The charge carrier lifetimes are on the order of hundreds of picoseconds, agreeing well with the experimental data.[95] The nonradiative charge recombination time is 2 times longer for the MAI-terminated system, compared to that of PbI_2 termination. Thus, the MAI termination is favorable for both charge separation and recombination, suggesting strongly that $MAPbI_3$ should be prepared under MAI rich conditions prior to its formation of interfaces with CuSCN and other HTMs.

To test the sensitivity of the conclusions of our work to simulation cell properties, including its size, symmetry, and slab construction, we constructed eight more systems (Figures S1−S8). The simulation cells shown in Figure 1 contain 272 atoms, exactly the same for both terminations. However, the top and bottom surfaces of the $MAPbI_3$ slab are different. We constructed $MAPbI_3$ slabs with symmetric terminations and large sizes, containing ≤942 atoms. The slab setups with vacuum contain one $MAPbI_3$/CuSCN interface and two surfaces, arising from contacts of $MAPbI_3$ and CuSCN with vacuum. Additionally, we considered simulation setups without vacuum and containing two $MAPbI_3$/CuSCN interfaces. The PDOS calculated for these simulations cells demonstrates the same type II band alignment as the original simulation cell, and the charge densities exhibit the same localizations, confirming that the MAI termination favors fast hole transfer and slow electron−hole recombination. The key conclusions are independent of simulation cell details, because they depend on the general properties of $MAPbI_3$. In particular, because holes in $MAPbI_3$ are supported by iodine atoms, the direct contact of iodines with CuSCN facilitates rapid hole transfer for MAI termination. In contrast, electrons in $MAPbI_3$ are supported by Pb atoms, and spatial separation of $MAPbI_3$ electrons from CuSCN holes at the MAI-terminated interface favors slow charge recombination.

Note that our simulations focus on the interfacial dynamics and do not consider charge diffusion, which occurs over scales that are much larger than any *ab initio* calculation can afford.

In summary, we have carried out time-domain *ab initio* simulations of photoinduced hole transfer and electron−hole recombination in the $MAPbI_3$/CuSCN heterojunctions with different terminations of the $MAPbI_3$ surface. The calculations show that $MAPbI_3$ termination has a strong influence on both charge separation and recombination. Fortunately, both processes benefit from MAI termination, which favors rapid charge separation and slow recombination. Termination of the $MAPbI_3$ surface has an only minor influence on the alignment of relevant energy levels and gaps; however, it changes the charge separation time by a factor of 1.5 and the charge recombination time by a factor of 2. The charge separation is faster for the MAI termination, because holes in $MAPbI_3$ are localized on iodine atoms, which are present in the MAI terminating layer, and because rapid motions of the interfacial MA cations influence holes via electrostatic interactions as holes pass through the interface region. Crossings of the donor and acceptor energy levels become more frequent, and the hole transfer accelerates. Importantly, the injected hole remains hot for 200−300 fs, and the hot hole can escape the interfacial region prior to forming a bound state with the remaining electron. This situation is particularly favorable when holes are extrated by organic layers, such as spiro-MeOTAD, which are prone to forming strongly bound excitons due to low dielectric constants and weak screening of electrostatic electron−hole interactions. The charge separation is slower for the MAI termination of $MAPbI_3$, because the PbI_2-terminated $MAPbI_3$ surface forms more chemical bonds with CuSCN, and because electrons in $MAPbI_3$ are localized on Pb atoms and remain farther from the interface in the MAI-terminated $MAPbI_3$. Obtained for the CuSCN hole transport layer, these conclusions should hold for other HTMs, as well, because they rely completely on the properties of the $MAPbI_3$ surfaces. One can also expect that the conclusions apply to other hybrid organic−inorganic halide perovskites, in which MA, Pb, or I is replaced with different species. The conclusions regarding the charge recombination should hold for all-inorganic perovksites, as well. Whether the hole transfer results apply to all-inorganic perovskites requires further investigation, because the hole transfer depends on the properties of the organic cation. The study strongly suggests that $MAPbI_3$ should be treated with extra MAI prior to it forming interfaces with HTMs and provides a detailed atomistic rationalization for this recommendation. This concrete design principle should hold generally for perovskite interfaces with most hole-accepting layers, allowing one to improve the performance of metal halide perovskite solar cells and related devices.

■ ASSOCIATED CONTENT

Supporting Information

The Supporting Information is available free of charge at https://pubs.acs.org/doi/10.1021/acs.jpclett.0c01467.

Ensemble-averaged absolute values of NA couplings between adjacent VB states of the MAI- and PbI_2-terminated $MAPbI_3$/CuSCN heterojunctions and densities of states and charge densities of key states in larger simulation cells with symmetric termination of the $MAPbI_3$ slabs (PDF)

■ AUTHOR INFORMATION

Corresponding Author

Run Long − *College of Chemistry, Key Laboratory of Theoretical & Computational Photochemistry of Ministry of Education, Beijing Normal University, Beijing 100875, P. R. China;*

https://dx.doi.org/10.1021/acs.jpclett.0c01467
J. Phys. Chem. Lett. 2020, 11, 4481−4489

orcid.org/0000-0003-3912-8899; Email: runlong@bnu.edu.cn

Authors

Jinlu He — *College of Chemistry, Key Laboratory of Theoretical & Computational Photochemistry of Ministry of Education, Beijing Normal University, Beijing 100875, P. R. China*

David Casanova — *Donostia International Physics Center (DIPC), 20018 Donostia, Euskadi, Spain; IKERBASQUE, Basque Foundation for Science, 48013 Bilbao, Euskadi, Spain;* orcid.org/0000-0002-8893-7089

Wei-Hai Fang — *College of Chemistry, Key Laboratory of Theoretical & Computational Photochemistry of Ministry of Education, Beijing Normal University, Beijing 100875, P. R. China;* orcid.org/0000-0002-1668-465X

Oleg V. Prezhdo — *Department of Chemistry, University of Southern California, Los Angeles, California 90089, United States;* orcid.org/0000-0002-5140-7500

Complete contact information is available at:
https://pubs.acs.org/10.1021/acs.jpclett.0c01467

Notes

The authors declare no competing financial interest.

■ ACKNOWLEDGMENTS

J.H., W.-H.F., and R.L. acknowledge support by the National Natural Science Foundation of China (Grants 21573022, 51861135101, 21590801, 21520102005, and 21688102). R.L. acknowledges financial support by the Fundamental Research Funds for the Central Universities, the Recruitment Program of Global Youth Experts of China, and the Beijing Normal University Startup. D.C. acknowledges the Spanish Government MINECO/FEDER (Project CTQ2016-80955-P). O.V.P. acknowledges funding from the U.S. National Science Foundation (Grant CHE-1900510) and is grateful to Beijing Normal University for hospitality during manuscript preparation.

■ REFERENCES

(1) Yang, W. S.; Noh, J. H.; Jeon, N. J.; Kim, Y. C.; Ryu, S.; Seo, J.; Seok, S. I. High-Performance Photovoltaic Perovskite Layers Fabricated through Intramolecular Exchange. *Science* **2015**, *348*, 1234−1237.

(2) Shang, M.-H.; Zhang, J.; Zhang, P.; Yang, Z.; Zheng, J.; Haque, M. A.; Yang, W.; Wei, S.-H.; Wu, T. Stable Bandgap-Tunable Hybrid Perovskites with Alloyed Pb−Ba Cations for High-Performance Photovoltaic Applications. *J. Phys. Chem. Lett.* **2019**, *10*, 59−66.

(3) Alarousu, E.; El-Zohry, A. M.; Yin, J.; Zhumekenov, A. A.; Yang, C.; Alhabshi, E.; Gereige, I.; AlSaggaf, A.; Malko, A. V.; Bakr, O. M.; Mohammed, O. F. Ultralong Radiative States in Hybrid Perovskite Crystals: Compositions for Submillimeter Diffusion Lengths. *J. Phys. Chem. Lett.* **2017**, *8*, 4386−4390.

(4) Gong, X.; Yang, Z.; Walters, G.; Comin, R.; Ning, Z.; Beauregard, E.; Adinolfi, V.; Voznyy, O.; Sargent, E. H. Highly Efficient Quantum Dot near-Infrared Light-Emitting Diodes. *Nat. Photonics* **2016**, *10*, 253−257.

(5) Fu, Y.; Zhu, H.; Schrader, A. W.; Liang, D.; Ding, Q.; Joshi, P.; Hwang, L.; Zhu, X.; Jin, S. Nanowire Lasers of Formamidinium Lead Halide Perovskites and Their Stabilized Alloys with Improved Stability. *Nano Lett.* **2016**, *16*, 1000−1008.

(6) Chen, Y.-S.; Manser, J. S.; Kamat, P. V. All Solution-Processed Lead Halide Perovskite-$Bivo_4$ Tndem Assembly for Photolytic Solar Fuels Production. *J. Am. Chem. Soc.* **2015**, *137*, 974−981.

(7) Zhao, Y.; Zhu, K. Solution Chemistry Engineering toward High-Efficiency Perovskite Solar Cells. *J. Phys. Chem. Lett.* **2014**, *5*, 4175−4186.

(8) Anaya, M.; Lozano, G.; Calvo, M. E.; Zhang, W.; Johnston, M. B.; Snaith, H. J.; Míguez, H. Optical Description of Mesostructured Organic−Inorganic Halide Perovskite Solar Cells. *J. Phys. Chem. Lett.* **2015**, *6*, 48−53.

(9) Liu, X.; Xiao, Y.; Zeng, Q.; Jiang, J.; Li, Y. Large-Area Organic-Free Perovskite Solar Cells with High Thermal Stability. *J. Phys. Chem. Lett.* **2019**, *10*, 6382−6388.

(10) Kulbak, M.; Gupta, S.; Kedem, N.; Levine, I.; Bendikov, T.; Hodes, G.; Cahen, D. Cesium Enhances Long-Term Stability of Lead Bromide Perovskite-Based Solar Cells. *J. Phys. Chem. Lett.* **2016**, *7*, 167−172.

(11) Kojima, A.; Teshima, K.; Shirai, Y.; Miyasaka, T. Organometal Halide Perovskites as Visible-Light Sensitizers for Photovoltaic Cells. *J. Am. Chem. Soc.* **2009**, *131*, 6050−6051.

(12) Efficiency Chart. https://www.nrel.gov/pv/cell-efficiency.html, 2019 (accessed on May 15, 2019).

(13) Burschka, J.; Pellet, N.; Moon, S.-J.; Humphry-Baker, R.; Gao, P.; Nazeeruddin, M. K.; Grätzel, M. Sequential Deposition as a Route to High-Performance Perovskite-Sensitized Solar Cells. *Nature* **2013**, *499*, 316−319.

(14) Jeon, N. J.; Noh, J. H.; Yang, W. S.; Kim, Y. C.; Ryu, S.; Seo, J.; Seok, S. I. Compositional Engineering of Perovskite Materials for High-Performance Solar Cells. *Nature* **2015**, *517*, 476−480.

(15) Qin, P.; Tanaka, S.; Ito, S.; Tetreault, N.; Manabe, K.; Nishino, H.; Nazeeruddin, M. K.; Grätzel, M. Inorganic Hole Conductor-Based Lead Halide Perovskite Solar Cells with 12.4% Conversion Efficiency. *Nat. Commun.* **2014**, *5*, 3834.

(16) Park, J. H.; Seo, J.; Park, S.; Shin, S. S.; Kim, Y. C.; Jeon, N. J.; Shin, H. W.; Ahn, T. K.; Noh, J. H.; Yoon, S. C.; Hwang, C. S.; Seok, S. I. Efficient Ch_3 nh_3 pbi_3 Perovskite Solar Cells Employing Nanostructured P-Type Nio Electrode Formed by a Pulsed Laser Deposition. *Adv. Mater.* **2015**, *27*, 4013−4019.

(17) Christians, J. A.; Fung, R. C.; Kamat, P. V. An Inorganic Hole Conductor for Organo-Lead Halide Perovskite Solar Cells. Improved Hole Conductivity with Copper Iodide. *J. Am. Chem. Soc.* **2014**, *136*, 758−764.

(18) Arora, N.; Dar, M. I.; Hinderhofer, A.; Pellet, N.; Schreiber, F.; Zakeeruddin, S. M.; Grätzel, M. Perovskite Solar Cells with Cuscn Hole Extraction Layers Yield Stabilized Efficiencies Greater Than 20%. *Science* **2017**, *358*, 768−771.

(19) Zhao, K.; Munir, R.; Yan, B.; Yang, Y.; Kim, T.; Amassian, A. Solution-Processed Inorganic Copper (I) Thiocyanate (Cuscn) Hole Transporting Layers for Efficient P−I−N Perovskite Solar Cells. *J. Mater. Chem. A* **2015**, *3*, 20554−20559.

(20) Madhavan, V. E.; Zimmermann, I.; Roldán-Carmona, C.; Grancini, G.; Buffiere, M.; Belaidi, A.; Nazeeruddin, M. K. Copper Thiocyanate Inorganic Hole-Transporting Material for High-Efficiency Perovskite Solar Cells. *ACS Energy Lett.* **2016**, *1*, 1112−1117.

(21) Jung, M.; Kim, Y. C.; Jeon, N. J.; Yang, W. S.; Seo, J.; Noh, J. H.; Il Seok, S. Thermal Stability of Cuscn Hole Conductor-Based Perovskite Solar Cells. *ChemSusChem* **2016**, *9*, 2592−2596.

(22) Jaffe, J. E.; Kaspar, T. C.; Droubay, T. C.; Varga, T.; Bowden, M. E.; Exarhos, G. J. Electronic and Defect Structures of Cuscn. *J. Phys. Chem. C* **2010**, *114*, 9111−9117.

(23) Leng, J.; Liu, J.; Zhang, J.; Jin, S. Decoupling Interfacial Charge Transfer from Bulk Diffusion Unravels Its Intrinsic Role for Efficient Charge Extraction in Perovskite Solar Cells. *J. Phys. Chem. Lett.* **2016**, *7*, 5056−5061.

(24) Chen, B.; Hu, H.; Salim, T.; Lam, Y. M. A Facile Method to Evaluate the Influence of Trap Densities on Perovskite Solar Cell Performance. *J. Mater. Chem. C* **2019**, *7*, 5646−5651.

(25) Mosconi, E.; Grancini, G.; Roldán-Carmona, C.; Gratia, P.; Zimmermann, I.; Nazeeruddin, M. K.; De Angelis, F. Enhanced $Tio_{2/M}$ $apbi_3$ Electronic Coupling by Interface Modification with Pbi_2. *Chem. Mater.* **2016**, *28*, 3612−3615.

(26) Quarti, C.; De Angelis, F.; Beljonne, D. Influence of Surface Termination on the Energy Level Alignment at the Ch_3 nh_3 pbi_3 Perovskite/C60 Interface. *Chem. Mater.* **2017**, *29*, 958−968.
(27) Parandekar, P. V.; Tully, J. C. Mixed Quantum-Classical Equilibrium. *J. Chem. Phys.* **2005**, *122*, 094102.
(28) Tully, J. C. Molecular Dynamics with Electronic Transitions. *J. Chem. Phys.* **1990**, *93*, 1061−1071.
(29) Akimov, A. V.; Prezhdo, O. V. The Pyxaid Program for Non-Adiabatic Molecular Dynamics in Condensed Matter Systems. *J. Chem. Theory Comput.* **2013**, *9*, 4959−4972.
(30) Kohn, W.; Sham, L. J. Self-Consistent Equations Including Exchange and Correlation Effects, J. Phys. Rev. A 140, 1133 (1965). *Phys. Rev.* **1965**, *140*, A1133−A1138.
(31) Craig, C. F.; Duncan, W. R.; Prezhdo, O. V. Trajectory Surface Hopping in the Time-Dependent Kohn-Sham Approach for Electron-Nuclear Dynamics. *Phys. Rev. Lett.* **2005**, *95*, 163001.
(32) Habenicht, B. F.; Prezhdo, O. V. Nonradiative Quenching of Fluorescence in a Semiconducting Carbon Nanotube: A Time-Domain Ab Initio Study. *Phys. Rev. Lett.* **2008**, *100*, 197402.
(33) Bittner, E. R.; Rossky, P. J. Quantum Decoherence in Mixed Quantum-Classical Systems: Nonadiabatic Processes. *J. Chem. Phys.* **1995**, *103*, 8130−8143.
(34) Schwartz, B. J.; Bittner, E. R.; Prezhdo, O. V.; Rossky, P. J. Quantum Decoherence and the Isotope Effect in Condensed Phase Nonadiabatic Molecular Dynamics Simulations. *J. Chem. Phys.* **1996**, *104*, 5942−5955.
(35) Zhu, C.; Nangia, S.; Jasper, A. W.; Truhlar, D. G. Coherent Switching with Decay of Mixing: An Improved Treatment of Electronic Coherence for Non-Born-Oppenheimer Trajectories. *J. Chem. Phys.* **2004**, *121*, 7658−7670.
(36) Mukamel, S. *Principles of Nonlinear Optical Spectroscopy*; Oxford University Press, 1995.
(37) Akimov, A. V.; Prezhdo, O. V. Persistent Electronic Coherence Despite Rapid Loss of Electron-Nuclear Correlation. *J. Phys. Chem. Lett.* **2013**, *4*, 3857−3864.
(38) He, J.; Fang, W.-H.; Long, R.; Prezhdo, O. V. Increased Lattice Stiffness Suppresses Nonradiative Charge Recombination in $Mapbi_3$ Doped with Larger Cations: Time-Domain Ab Initio Analysis. *ACS Energy Lett.* **2018**, *3*, 2070−2076.
(39) Wang, Y.; Long, R. Unravelling the Effects of Pressure-Induced Suppressed Electron-Hole Recombination in Cspbbr3 Perovskite: Time-Domain Ab Initio Analysis. *J. Phys. Chem. Lett.* **2019**, *10*, 4354−4361.
(40) Qiao, L.; Fang, W.-H.; Long, R. Dopant Control of Electron−Hole Recombination in Cesium−Titanium Halide Double Perovskite by Time Domain Ab Initio Simulation: Codoping Supersedes Monodoping. *J. Phys. Chem. Lett.* **2018**, *9*, 6907−6914.
(41) Qiao, L.; Sun, X.; Long, R. Mixed Cs and Fa Cations Slow Electron-Hole Recombination in $Fapbi_3$ Perovskite by Time-Domain Ab Initio Study: Lattice Contraction Versus Octahedral Tilting. *J. Phys. Chem. Lett.* **2019**, *10*, 672−678.
(42) Li, W.; Sun, Y.-Y.; Li, L.; Zhou, Z.; Tang, J.; Prezhdo, O. V. Control of Charge Recombination in Perovskites by Oxidation State of Halide Vacancy. *J. Am. Chem. Soc.* **2018**, *140*, 15753−15763.
(43) He, J. L.; Vasenko, A. S.; Long, R.; Prezhdo, O. V. Halide Composition Controls Electron-Hole Recombination in Cesium-Lead Halide Perovskite Quantum Dots: A Time Domain Ab Lnitio Study. *J. Phys. Chem. Lett.* **2018**, *9*, 1872−1879.
(44) Wang, S. Y.; Luo, Q. Q.; Fang, W. H.; Long, R. Interfacial Engineering Determines Band Alignment and Steers Charge Separation and Recombination at an Inorganic Perovskite Quantum Dot/Ws_2 Junction: A Time Domain Ab Initio Study. *J. Phys. Chem. Lett.* **2019**, *10*, 1234−1241.
(45) He, J. L.; Fang, W. H.; Long, R.; Prezhdo, O. V. Superoxide/Peroxide Chemistry Extends Charge Carriers' Lifetime but Undermines Chemical Stability of Ch_3 nh_3 pbi_3 Exposed to Oxygen: Time-Domain Ab Initio Analysis. *J. Am. Chem. Soc.* **2019**, *141*, 5798−5807.
(46) Li, W.; Long, R.; Tang, J. F.; Prezhdo, O. V. Influence of Defects on Excited-State Dynamics in Lead Halide Perovskites: Time-Domain Ab Initio Studies. *J. Phys. Chem. Lett.* **2019**, *10*, 3788−3804.
(47) Li, W.; Tang, J. F.; Casanova, D.; Prezhdo, O. V. Time-Domain Ab Lnitio Analysis Rationalizes the Unusual Temperature Dependence of Charge Carrier Relaxation in Lead Halide Perovskite. *ACS Energy Lett.* **2018**, *3*, 2713−2720.
(48) Wang, Y. T.; Fang, W. H.; Long, R.; Prezhdo, O. V. Symmetry Breaking at Mapbi(3) Perovskite Grain Boundaries Suppresses Charge Recombination: Time-Domain Ab Initio Analysis. *J. Phys. Chem. Lett.* **2019**, *10*, 1617−1623.
(49) Zhang, Z. S.; Fang, W. H.; Tokina, M. V.; Long, R.; Prezhdo, O. V. Rapid Decoherence Suppresses Charge Recombination in Multi-Layer 2d Halide Perovskites: Time-Domain Ab Initio Analysis. *Nano Lett.* **2018**, *18*, 2459−2466.
(50) Zhang, Z. S.; Long, R.; Tokina, M. V.; Prezhdo, O. V. Interplay between Localized and Free Charge Carriers Can Explain Hot Fluorescence in the $Ch3nh3pbbr_3$ Perovskite: Time-Domain Ab Initio Analysis. *J. Am. Chem. Soc.* **2017**, *139*, 17327−17333.
(51) Jankowska, J.; Prezhdo, O. V. Ferroelectric Alignment of Organic Cations Inhibits Nonradiative Electron-Hole Recombination in Hybrid Perovskites: Ab Initio Nonadiabatic Molecular Dynamics. *J. Phys. Chem. Lett.* **2017**, *8*, 812−818.
(52) Li, W.; Liu, J.; Bai, F. Q.; Zhang, H. X.; Prezhdo, O. V. Hole Trapping by Iodine Interstitial Defects Decreases Free Carrier Losses in Perovskite Solar Cells: A Time-Domain Ab Initio Study. *ACS Energy Lett.* **2017**, *2*, 1270−1278.
(53) Liu, J.; Prezhdo, O. V. Chlorine Doping Reduces Electron-Hole Recombination in Lead Iodide Perovskites: Time-Domain Ab Initio Analysis. *J. Phys. Chem. Lett.* **2015**, *6*, 4463−4469.
(54) Li, W.; Vasenko, A. S.; Tang, J. F.; Prezhdo, O. V. Anharmonicity Extends Carrier Lifetimes in Lead Halide Perovskites at Elevated Temperatures. *J. Phys. Chem. Lett.* **2019**, *10*, 6219−6226.
(55) Wei, Y.; Long, R. Grain Boundaries Are Benign and Suppress Nonradiative Electron−Hole Recombination in Monolayer Black Phosphorus: A Time-Domain Ab Initio Study. *J. Phys. Chem. Lett.* **2018**, *9*, 3856−3862.
(56) Zhang, L. L.; Vasenko, A. S.; Zhao, J.; Prezhdo, O. V. Mono-Elemental Properties of 2d Black Phosphorus Ensure Extended Charge Carrier Lifetimes under Oxidation: Time-Domain Ab Initio Analysis. *J. Phys. Chem. Lett.* **2019**, *10*, 1083−1091.
(57) Wang, S. Y.; Fang, W. H.; Long, R. Hydrogen Passivated Silicon Grain Boundaries Greatly Reduce Charge Recombination for Improved Silicon/Perovskite Tandem Solar Cell Performance: Time Domain Ab Initio Analysis. *J. Phys. Chem. Lett.* **2019**, *10*, 2445−2452.
(58) Jankowska, J.; Prezhdo, O. V. Real-Time Atomistic Dynamics of Energy Flow in an Stm Setup: Revealing the Mechanism of Current-Induced Molecular Emission. *J. Phys. Chem. Lett.* **2018**, *9*, 3591−3597.
(59) Li, L. Q.; Long, R.; Prezhdo, O. V. Why Chemical Vapor Deposition Grown Mos_2 Samples Outperform Physical Vapor Deposition Samples: Time-Domain Ab Initio Analysis. *Nano Lett.* **2018**, *18*, 4008−4014.
(60) Li, W.; Long, R.; Hou, Z. F.; Tang, J. F.; Prezhdo, O. V. Influence of Encapsulated Water on Luminescence Energy, Line Width, and Lifetime of Carbon Nanotubes: Time Domain Ab Initio Analysis. *J. Phys. Chem. Lett.* **2018**, *9*, 4006−4013.
(61) Zhang, Z. S.; Liu, L. H.; Fang, W. H.; Long, R.; Tokina, M. V.; Prezhdo, O. V. Plasmon-Mediated Electron Injection from Au Nanorods into Mos_2: Traditional Versus Photoexcitation Mechanism. *Chem.* **2018**, *4*, 1112−1127.
(62) Zhou, X.; Jankowska, J.; Li, L. Q.; Giri, A.; Hopkins, P. E.; Prezhdo, O. V. Strong Influence of Ti Adhesion Layer on Electron-Phonon Relaxation in Thin Gold Films: Ab Initio Nonadiabatic Molecular Dynamics. *ACS Appl. Mater. Interfaces* **2017**, *9*, 43343−43351.
(63) Zhou, Z. H.; Liu, J.; Long, R.; Li, L. G.; Guo, L. J.; Prezhdo, O. V. Control of Charge Carriers Trapping and Relaxation in Hematite

by Oxygen Vacancy Charge: Ab Initio Non-Adiabatic Molecular Dynamics. *J. Am. Chem. Soc.* **2017**, *139*, 6707−6717.
(64) Li, L. Q.; Long, R.; Prezhdo, O. V. Charge Separation and Recombination in Two-Dimensional Mos_2/Ws_2: Time-Domain Ab Initio Modeling. *Chem. Mater.* **2017**, *29*, 2466−2473.
(65) Fischer, S. A.; Duncan, W. R.; Prezhdo, O. V. Ab Initio Nonadiabatic Molecular Dynamics of Wet-Electrons on the Tio_2 Surface. *J. Am. Chem. Soc.* **2009**, *131*, 15483−15491.
(66) Hyeon-Deuk, K.; Prezhdo, O. V. Multiple Exciton Generation and Recombination Dynamics in Small Si and Cdse Quantum Dots: An Ab Initio Time-Domain Study. *ACS Nano* **2012**, *6*, 1239−1250.
(67) Kilin, D. S.; Tsemekhman, K.; Prezhdo, O. V.; Zenkevich, E. I.; von Borczyskowski, C. Ab Initio Study of Exciton Transfer Dynamics from a Core-Shell Semiconductor Quantum Dot to a Porphyrin-Sensitizer. *J. Photochem. Photobiol., A* **2007**, *190*, 342−351.
(68) Chaban, V. V.; Prezhdo, V. V.; Prezhdo, O. V. Covalent Linking Greatly Enhances Photoinduced Electron Transfer in Fullerene-Quantum Dot Nanocomposites: Time-Domain Ab Initio Study. *J. Phys. Chem. Lett.* **2013**, *4*, 1−6.
(69) Wang, L. J.; Long, R.; Prezhdo, O. V. Time-Domain Ab Initio Modeling of Photoinduced Dynamics at Nanoscale Interfaces. *Annu. Rev. Phys. Chem.* **2015**, *66*, 549−579.
(70) Akimov, A. V.; Prezhdo, O. V. Advanced Capabilities of the Pyxaid Program: Integration Schemes, Decoherence Effects, Multi-excitonic States, and Field-Matter Interaction. *J. Chem. Theory Comput.* **2014**, *10*, 789−804.
(71) Kresse, G.; Furthmüller, J. Efficient Iterative Schemes for Ab Initio Total-Energy Calculations Using a Plane-Wave Basis Set. *Phys. Rev. B: Condens. Matter Mater. Phys.* **1996**, *54*, 11169−11186.
(72) Perdew, J. P.; Burke, K.; Ernzerhof, M. Generalized Gradient Approximation Made Simple. *Phys. Rev. Lett.* **1996**, *77*, 3865−3868.
(73) Blochl, P. E. Projector Augmented-Wave Method. *Phys. Rev. B: Condens. Matter Mater. Phys.* **1994**, *50*, 17953−17979.
(74) Monkhorst, H. J.; Pack, J. D. Special Points for Brillouin-Zone Integrations. *Phys. Rev. B* **1976**, *13*, 5188−5192.
(75) Grimme, S.; Antony, J.; Ehrlich, S.; Krieg, H. A Consistent and Accurate Ab Initio Parametrization of Density Functional Dispersion Correction (Dft-D) for the 94 Elements H-Pu. *J. Chem. Phys.* **2010**, *132*, 154104.
(76) Long, R.; Liu, J.; Prezhdo, O. V. Unravelling the Effects of Grain Boundary and Chemical Doping on Electron−Hole Recombination in Ch_3 nh_3 pbi_3 Perovskite by Time-Domain Atomistic Simulation. *J. Am. Chem. Soc.* **2016**, *138*, 3884−3890.
(77) Long, R.; Fang, W.; Prezhdo, O. V. Moderate Humidity Delays Electron−Hole Recombination in Hybrid Organic−Inorganic Perovskites: Time-Domain Ab Initio Simulations Rationalize Experiments. *J. Phys. Chem. Lett.* **2016**, *7*, 3215−3222.
(78) Long, R.; Prezhdo, O. V. Dopants Control Electron-Hole Recombination at Perovskite-Tio_2 Interfaces: Ab Initio Time-Domain Study. *ACS Nano* **2015**, *9*, 11143−11155.
(79) Tsetseris, L. Two-Dimensional Copper Thio-and Seleno-Cyanates. *Phys. Chem. Chem. Phys.* **2016**, *18*, 7837−7840.
(80) She, L.; Liu, M.; Zhong, D. Atomic Structures of Ch_3 nh_{3p} bi_3 (001) Surfaces. *ACS Nano* **2016**, *10*, 1126−1131.
(81) Quarti, C.; Grancini, G.; Mosconi, E.; Bruno, P.; Ball, J. M.; Lee, M. M.; Snaith, H. J.; Petrozza, A.; De Angelis, F. The Raman Spectrum of the Ch_3 nh_3 pbi_3 Hybrid Perovskite: Interplay of Theory and Experiment. *J. Phys. Chem. Lett.* **2014**, *5*, 279−284.
(82) Aldakov, D.; Chappaz-Gillot, C.; Salazar, R.; Delaye, V.; Welsby, K. A.; Ivanova, V.; Dunstan, P. R. Properties of Electrodeposited Cuscn 2d Layers and Nanowires Influenced by Their Mixed Domain Structure. *J. Phys. Chem. C* **2014**, *118*, 16095−16103.
(83) Akimov, A. V.; Prezhdo, O. V. Large-Scale Computations in Chemistry: A Bird's Eye View of a Vibrant Field. *Chem. Rev.* **2015**, *115*, 5797−5890.
(84) Prezhdo, O. V.; Rossky, P. J. Evaluation of Quantum Transition Rates from Quantum-Classical Molecular Dynamics Simulations. *J. Chem. Phys.* **1997**, *107*, 5863−5878.
(85) Prezhdo, O. V.; Rossky, P. J. Relationship between Quantum Decoherence Times and Solvation Dynamics in Condensed Phase Chemical Systems. *Phys. Rev. Lett.* **1998**, *81*, 5294−5297.
(86) Marcus, M.; Tozer, O. R.; Barford, W. Theory of Optical Transitions in Conjugated Polymers. Ii. Real Systems. *J. Chem. Phys.* **2014**, *141*, 164102.
(87) Habenicht, B. F.; Kalugin, O. N.; Prezhdo, O. V. Ab Initio Study of Phonon-Induced Denhasina of Electronic Excitations in Narrow Graphene Nanoribbons. *Nano Lett.* **2008**, *8*, 2510−2516.
(88) Habenicht, B. F.; Kamisaka, H.; Yamashita, K.; Prezhdo, O. V. Ab Initio Study of Vibrational Dephasing of Electronic Excitations in Semiconducting Carbon Nanotubes. *Nano Lett.* **2007**, *7*, 3260−3265.
(89) Madrid, A. B.; Hyeon-Deuk, K.; Habenicht, B. F.; Prezhdo, O. V. Phonon-Induced Dephasing of Excitons in Semiconductor Quantum Dots: Multiple Exciton Generation, Fission, and Luminescence. *ACS Nano* **2009**, *3*, 2487−2494.
(90) Guo, Z. Y.; Habenicht, B. F.; Liang, W. Z.; Prezhdo, O. V. Ab Initio Study of Phonon-Induced Dephasing of Plasmon Excitations in Silver Quantum Dots. *Phys. Rev. B: Condens. Matter Mater. Phys.* **2010**, *81*, 125415.
(91) Kamisaka, H.; Kilina, S. V.; Yamashita, K.; Prezhdo, O. V. Ab Initio Study of Temperature- and Pressure Dependence of Energy and Phonon-Induced Dephasing of Electronic Excitations in Cdse and Pbse Quantum Dots. *J. Phys. Chem. C* **2008**, *112*, 7800−7808.
(92) Liu, J.; Kilina, S. V.; Tretiak, S.; Prezhdo, O. V. Ligands Slow Down Pure-Dephasing in Semiconductor Quantum Dots. *ACS Nano* **2015**, *9*, 9106−9116.
(93) Pal, S.; Nijjar, P.; Frauenheim, T.; Prezhdo, O. V. Atomistic Analysis of Room Temperature Quantum Coherence in Two-Dimensional Cdse Nanostructures. *Nano Lett.* **2017**, *17*, 2389−2396.
(94) Kilina, S. V.; Neukirch, A. J.; Habenicht, B. F.; Kilin, D. S.; Prezhdo, O. V. Quantum Zeno Effect Rationalizes the Phonon Bottleneck in Semiconductor Quantum Dots. *Phys. Rev. Lett.* **2013**, *110*, 180404.
(95) Pydzińska, K.; Karolczak, J.; Kosta, I.; Tena-Zaera, R.; Todinova, A.; Idígoras, J.; Anta, J. A.; Ziółek, M. Determination of Interfacial Charge-Transfer Rate Constants in Perovskite Solar Cells. *ChemSusChem* **2016**, *9*, 1647−1659.

https://dx.doi.org/10.1021/acs.jpclett.0c01467
J. Phys. Chem. Lett. 2020, 11, 4481−4489